Formation and crystal growth of needle-like fluoroapatite in functional glass-ceramics

W. Höland,[a] C. Ritzberger,[a] E. Apel,[a] V. Rheinberger,[a] R. Nesper,[b] F. Krumeich,[b]
C. Mönster[c] and H. Eckert[c]

The objective of the study is to analyze the solid state reactions leading to the precipitation of fluoroapatite, $Ca_5(PO_4)_3F$, in two different functional glass-ceramic systems (labeled A and B) of interest for restorative dentistry. Combined X-ray diffraction (XRD), electron microscopy (SEM and TEM) and solid state nuclear magnetic resonance (NMR) are used to characterize the solid state reactions, leading to the formation of primary and secondary crystalline phases, as well as the structural changes occurring in the residual glass matrix during this process. The results indicate that, depending on the composition of the ceramic, fluoroapatite crystallization can proceed by different mechanisms: (1) precipitation in a parallel process accompanying the formation of rhenanite ($NaCaPO_4$) primary crystals (glass-ceramic A), and (2) formation from amorphous and/or disordered crystalline precursor phases that are already segregated within a phase separated glass matrix (glass-ceramic B). In the latter case, this disordered phase transforms by solid state reaction into fluoroapatite at high temperatures of heat treatment of the glass-ceramic. The needle-like morphology of fluoroapatite in glass-ceramics mimics the morphology of hydroxyl-carbonato apatite in human teeth.

1. Introduction

The controlled precipitation of hydroxyapatite ($Ca_5(PO_4)_3OH$) in biological systems is the key factor to control the bioactive behavior of inorganic glasses and glass-ceramics for bone substitution.[1–3] In comparison to hydroxyapatite, fluoroapatite ($Ca_5(PO_4)_3F$) is characterized by a much better durability. The crystal structure of fluoroapatite shows the fluorine ions in the center of Ca^{2+} triangles.[4–6] Glass-ceramics with fluoroapatite crystals are durable biomaterials, preferably for dental restoration. These materials do not show bioactivity. With regard to this application, a number of promising glass-ceramic systems have been developed in recent years by exploiting the principles of controlled nucleation and crystallization in various inorganic base glasses.[7,8,9]

A distinction is made between two general mechanisms of nucleation and crystallization in glasses that are used for the development of glass-ceramics: surface mechanisms and internal mechanisms. The formation of apatite in glass-ceramics is controlled by internal mechanisms.[10–12] In the nucleation process, glass-in-glass phase separation plays an important part. Apart from apatite, a second crystal phase can be grown in glass-ceramics, for example aluminosilicate leucite ($KAlSi_2O_6$), according to the double nucleation process and crystallization through surface reactions. For this type of surface crystallization, however, the process must be conducted with granulated glass.[13]

The objective of the present study was to analyze the phenomena and formation reactions of fluoroapatite in two different glass-ceramic compositions and to draw the necessary conclusions regarding the solid state mechanisms, in particular with regard to preliminary and secondary phase formation.

Glass-ceramic A (Table 1), which forms leucite and apatite after grain processing, contains rhenanite ($NaCaPO_4$) as a ternary phase. In the present study, however, this glass-ceramic was used to fabricate bulk samples. The thin leucite layer which formed on the surface of the samples was removed after the heat treatment with grinding instruments to make the fluoroapatite more readily accessible for analysis. Nevertheless, if this glass-ceramic is to be used for technical applications, leucite has to be formed through the controlled crystallization of granulated glass.[13]

Glass-ceramic B forms fluoroapatite without any secondary phases at high temperatures. Bulk samples were also produced with this glass-ceramic. The investigation of this glass-ceramic focused on the preliminary phase formation with relatively small amounts of CaO and P_2O_5 before the crystallization of fluoroapatite. As Na_2O is incorporated into both glass-ceramics to promote glass formation, the role of possible secondary crystal phases, *e.g.* rhenanite, in the phase formation process has to be examined. Therefore, a third glass-ceramic was analyzed as a reference sample, in particular as a comparison to the NMR results. For this purpose a rhenanite glass-ceramic, which was developed as a bioactive material for the replacement of bone, was included in the present study.[14] Rhenanite crystals were also characterized as weak interface substances to hydroxyapatite.[15] The NMR results obtained on these materials provide useful reference data for the characterization of the crystallization of rhenanite in ceramic systems.

[a]Research and Development, Ivoclar Vivadent AG, Li-9494 Schaan, Liechtenstein
[b]Inst. Anorganische Chemie, Eidgenössische Technische Hochschule Zürich, CH-8093 Zürich, Switzerland
[c]Inst. Physikalische Chemie, Universität Münster, D-48145 Münster, Germany

Table 1 Chemical compositions of the three base glasses used

		SiO$_2$	Li$_2$O	Al$_2$O$_3$	K$_2$O	P$_2$O$_5$	ZrO$_2$	Na$_2$O	CaO	F	B$_2$O$_3$	CeO$_2$	TiO$_2$	other
A	wt%	54.6	0.2	14.2	10.7	4	0.9	8.4	5	0.7	0.3	0.8	0.2	
	mol%	61.5	0.5	9.4	7.7	1.9	0.5	9.2	6	2.5	0.3	0.3	0.2	
B	wt%	67.6	0.5	12.8	8.6	1.2		5.7	2.8	0.8				
	mol%	72.6	1.1	8.1	5.9	0.5		5.9	3.2	2.7				
C	wt%	57.9				6		22.8	12.9	0.3				0.1
	mol%	58.9				2.6		22.5	14.1	1.9				

In the development of glass-ceramics for dental applications, internal nucleation processes have been specifically exploited to precipitate fluoroapatite crystals with a special needle-like morphology.[9,10] These glass-ceramics are durable biomaterials, which do not have bioactive characteristics, but which nevertheless exhibit very special optical, mechanical, thermal and chemical properties that mimic those of natural teeth and improve the service life of the material. In this specific application, the formation of needle-like fluoroapatite serves to control the optical properties, such as transmission and brightness (in technical terms: value) in particular, of the biomaterial.

The goal of this paper mandates the use of complementary techniques to provide structural and compositional characterization on different length scales. In the present study, we have used the combination of X-ray diffraction (XRD), electron microscopy and advanced solid state nuclear magnetic resonance (NMR) methods to characterize the crystallization mechanism of two glass-ceramic compositions that are significant for applications in restorative dentistry. While XRD provides straightforward identification of the crystalline phases formed, electron microscopy together with microanalysis offers a profound insight into positional variations in the composition, as well as the spatial relationship of the phases formed. Furthermore, solid state NMR techniques can provide element-selective, inherently quantitative structural information at the local level. This element of selectivity is particularly valuable in the present application, where fluoride and phosphate represent only a very minor part of the overall material. In addition, NMR can provide immensely detailed structural information of the glassy component(s), which is not available from diffraction methods. Finally, in recent years the development of sophisticated two-dimensional and double resonance techniques has enormously increased the informational content of NMR spectra, providing structural information of unprecedented detail. In the present manuscript this potential will be explored and exploited to develop a detailed fundamental description of the crystallization mechanism in these systems.

2. Experimental

The following raw materials were used to produce glass A and B: quartz, potassium carbonate, sodium carbonate, calcium carbonate, aluminium oxyhydroxyhydrate, aluminium metaphosphate, boron oxide, titanium oxide, zirconium oxide, cerium oxide and sodium fluoride. Both glasses were melted in a Pt–Rh10 crucible on a 50 ml scale (glass A: 1650 °C, glass B: 1600 °C for 90 min each). Subsequently, the glasses were quenched (200–300 K s^{-1}) on a preheated metal plate (500 °C). In the process, glass discs of approximately 10 cm in diameter and thickness approximately 7 mm were produced. The bulk samples,

Table 2 Annealing stages conducted for glasses A, B, and C

Base glass thermal treatment		
A	B	C
800 °C, 1 h	800 °C, 4 h	900 °C, 1 h
900 °C, 1 h		900 °C, 1 h + 900°C, 1 h
1000 °C, 1 h	1000 °C, 1 h	1000 °C, 1 h

which were produced in this way, were relaxed for further examination (T_g + 20 °C). The cooling rate was between 3–5 K min^{-1} down to room temperature. After this fabrication process, glass A was opaque, while glass B and the reference glass C had a transparent appearance.

Subsequently, samples measuring 10 × 10 × 7 mm were cut from the discs. The programs which were used for the thermal post treatment of the base glasses for the controlled microstructure formation of the glass-ceramics are shown in Table 2. Before the different glass-ceramics were analyzed, the samples of glass-ceramic A were ground to remove the thin layer of surface precipitated leucite crystals. As a result, favorable conditions were created, which allowed internal phase formation processes to be analyzed.

XRD

Glasses and glass-ceramics of type A and B were examined with room temperature X-ray diffraction (RT-XRD). Monolithic glass samples with dimensions of approximately 10 mm × 10 mm × 2 mm were fabricated. An AXS D 5005 diffractometer (Bruker, Germany) with Cu-K$_\alpha$ radiation was used to perform the measurements in the range of $2\theta = 10.0$–$60.0°$.

TEM

Selected area electron diffraction (SAED) and transmission electron microscopy (TEM) investigations were performed with a CM30ST microscope (FEI; LaB$_6$ cathode, operated at 300 kV, point resolution ~2 Å). For scanning transmission electron microscopy (STEM), a Tecnai F30 microscope (FEI; field emission cathode, operated at 300 kV) equipped with a high-angle annular dark field (HAADF) STEM detector and an energy dispersive X-ray spectroscopy (EDXS) detector (EDAX) was used. After the focused electron beam was directed onto selected spots or small areas in the STEM image, the EDX spectrum was recorded (measuring time ~20–60 s), allowing us to perform a qualitative analysis there.

The procedure and equipment for preparing the electron microscopy samples has been described in detail elsewhere.[16] A

rectangular piece (approximately $1.5 \times 1.5 \times 15$ mm³) was cut from the glass-ceramic and embedded in a Cu pipe (diameter ~3 mm). After cutting ~300 μm thick discs and grinding and polishing them on both sides to a thickness of 100–150 μm, a dimple was ground on one or both sides to reach a thickness in the center of 20–30 μm. In the final step, milling with argon ions (PIPS, Gatan) was performed until a hole in the center of the samples was formed. The area adjacent to the hole was then thin enough for TEM and STEM investigations.

Thermal analysis characterization

All the samples were characterized by differential thermal analysis using a Netzsch STA 409 apparatus, operated at a heating rate of 10 K min⁻¹. The presence of crystalline $NaCaPO_4$ was detected by a sharp endotherm near 650 °C, signifying a first-order solid-to-solid phase transformation.

Solid state NMR

^{31}P solid state NMR spectra were obtained at 202.5 MHz on a Bruker Avance DSX-500 spectrometer equipped with a 4 mm MAS NMR probe operated at a spinning frequency of 15 kHz. Data were acquired with 90° pulses of 9–10 μs length. ^{31}P NMR spectra of glass C were obtained at 162.0 MHz on a Bruker Avance DSX-400 spectrometer at a spinning frequency of 12 kHz and 90° pulses of 1–2.5 μs length. Relaxation delays were chosen so as to yield representative spectra for the glassy components and the crystallized materials; this required values between 90 and 600 s in the different samples examined. Chemical shifts were reported relative to 85% H_3PO_4.

^{19}F MAS NMR spectra were acquired on a Bruker DSX-400 spectrometer at 188.3 MHz in a 4.65 T magnet. Samples were spun in 2.5 mm rotors at a spinning frequency of 25 kHz. To suppress ^{19}F background signals, a rotor-synchronized echo pulse sequence was used. The 90° pulse length in these experiments was 2.4–2.5 μs. A total of 1400–15500 scans were acquired. At least 13000 scans were necessary to detect the fluoroapatite (FAP) signal in base glass B. Experiments with different relaxation delays conducted on the FAP reference sample showed that a relaxation delay of 4 s was sufficient. Chemical shifts were externally referenced to solid AlF_3, taken as −172 ppm relative to the more common standard of $CFCl_3$.

To probe for the presence and strength of heteronuclear dipole–dipole couplings, the pulse sequences REDOR (rotational echo double resonance) and TRAPDOR (transfer of populations with double resonance) were used.[17] The heterodipolar coupling between the nuclear spin species S (whose signal is detected) and spatially close nuclear spin species I is normally averaged out by MAS. However, it can be reintroduced into the experiment by coherent I-spin irradiation during the rotor period. In an S{I} REDOR experiment, where both nuclei are spin $-\frac{1}{2}$, this is done by applying π-pulses on the I channel in the middle of the rotor period (sequence of Schaefer and Gullion[18]). For $S = \frac{1}{2}$, $I > \frac{1}{2}$ nuclei the REDOR sequence of Garbow and Gullion,[19] which applies the recoupling π-pulses to the observed nucleus S, is preferred. ^{19}F{^{23}Na} dipolar recoupling was done using the TRAPDOR experiment.[17] The latter utilizes continuous-wave irradiation of the ^{23}Na nuclei under MAS conditions, while the

Table 3 Experimental conditions used in the double-resonance NMR experiments

	Combination				
	^{31}P{^{23}Na}	^{31}P{^{19}F}	^{31}P{^{27}Al}	^{19}F{^{31}P}	^{19}F{^{23}Na}
Expt	REDOR	REDOR	TRAPDOR	REDOR	TRAPDOR
ν_r/kHz[a]	14000	14000	14000	15000	15000
ν_0(S)/MHz[b]	202.5	162.0	202.5	376.6	376.6
ν_0(I)/MHz[c]	132.3	376.6	130.3	162.0	105.9
$\tau_{90°}$(S)/μs[d]	2.8–2.9	2.2	10.1	2.2–2.5	2.2–2.5
$\tau_{90°}$(I)/μs[e]	2.2–2.4	2.1		2.0–2.4	
T_D/ms[f]	1.0–1.4	1.0–1.6	1.0	1.5	0.7
T_R/s[g]	90–110	90	90	4	4

[a] MAS rotor frequency. [b] S-spin resonance frequency. [c] I-spin resonance frequency. [d] S-spin 90° pulse length. [e] I-spin 90° pulse length. [f] Dephasing delay. [g] Relaxation delay.

^{19}F signals are detected by a rotor-synchronized spin echo sequence.

In all of these double resonance experiments, the presence of heteronuclear dipole–dipole interactions produces a decrease in S-spin signal intensity, relative to a reference experiment without I-spin irradiation (intensity S_0). The magnitude $(S_0 - S)/S_0$ of the difference signal depends on both the strength of the dipole–dipole coupling and on the length NT_r (number or rotor cycle time duration of one rotor period) of the overall dipolar evolution time. In general, REDOR experiments lend themselves to a more straightforward quantitative analysis, whereas TRAPDOR experiments are more effective in the case of quadrupolar I nuclei. ^{31}P{^{23}Na} REDOR studies were conducted on a Bruker DSX-500 spectrometer equipped with a 4 mm ^{31}P–X double resonance probe, while the double-resonance experiments involving ^{19}F nuclei were done on a Bruker DSX-400 spectrometer using a 4 mm ^{19}F–X probe. Table 3 gives a summary of the specific conditions used in the different double resonance experiments. In the present application, the low phosphorus content of our samples precluded the obtention of full REDOR curves $(S_0 - S)/S_0$ (NT_r). Rather, the difference signal was measured at a fixed dipolar evolution time (1 to 1.6 ms) and compared with corresponding values measured under the same conditions on the reference compounds $NaCaPO_4$ and $Ca_5(PO_4)_3F$, for a quantitative assessment of dipolar interaction strengths.

3. Results and discussion

3.1. Compositions and thermal treatment of base glasses

The chemical compositions of the two glass-ceramic materials A and B containing needle-like fluoroapatite crystals are shown in Table 1 according to chemical analysis. Likewise, Table 1 contains the chemical composition of the reference glass-ceramic C. The comparison between glass-ceramics A and B clearly shows that glass-ceramic A is a multi-component system. The contents of CaO and P_2O_5 are higher than those in glass-ceramic B. Furthermore, the Na_2O content is also higher than in glass-ceramic B. These are important prerequisites for examining the phase formation processes of glass-ceramics. The reference glass-ceramic C does not contain any Al_2O_3 and the contents of CaO and Na_2O are significantly higher than in systems A or B.

Glass-ceramics of type A are known as functional biomaterials, which are used to veneer dental frameworks made of metal. Glass-ceramics of type B are known as functional materials, which are used to veneer metal-free dental restoratives: for example, high strength lithium disilicate glass-ceramics or sintered ZrO_2 ceramic frameworks.

The possible primary crystal phase formation of the base glasses and the microstructure of the samples were investigated in detail by X-ray diffraction (XRD), scanning electron microscopy (SEM) and nuclear magnetic resonance (NMR). Based on these results, the base glass A in the form of bulk samples was heat treated according to the parameters given in Table 2.

3.2. Phase formation in glass and glass-ceramic A

3.2.1. X-Ray powder diffraction results. After casting and cooling of the melt, the base glass looked like a typical opaque glass. This appearance is characteristic of phase separated glasses. However, in the XRD pattern (Fig 1) the crystal phase of rhenanite ($NaCaPO_4$) is clearly detectable. According to this finding, the glass melt has to be characterized as a liquid that is highly supersaturated with Na^+, Ca^{2+} and PO_4^{3-} ions, which form crystals as the glass cools.

The precipitation of fluoroapatite in the glass-ceramic was determined by XRD after thermal treatment at 800 °C for 1 h. The main X-ray intensity diffraction peaks correspond to $Ca_5(PO_4)_3F$, according to JCPDS 00-015-0876.

3.2.2. Microstructure. First, microstructure investigations of the base glasses and the heat treated samples were conducted with a scanning electron microscope (SEM). The microstructure of the base glass already shows a crystal phase of rhenanite in the XRD examination. Previous results of rhenanite-containing glass-ceramics had shown that it is difficult to analyze the microstructure of this type of material without etching the samples.[9] If the samples are etched, however, this procedure and the selective reaction behavior associated with it have to be taken into consideration in the interpretation of the SEM images. In the present study, two etching procedures were selected (section 2). Fig. 2a shows the microstructure after HF etching. Holes of different geometries, ranging from approximately 20 nm up to 70 nm, are visible. In addition, small particles of approximately 50 nm were detected as agglomerates at different locations of the sample. Some of the latter are located in the etched holes. In contrast to the situation in the HF etched sample, Fig. 2b shows individual circular holes with a regular diameter of approximately
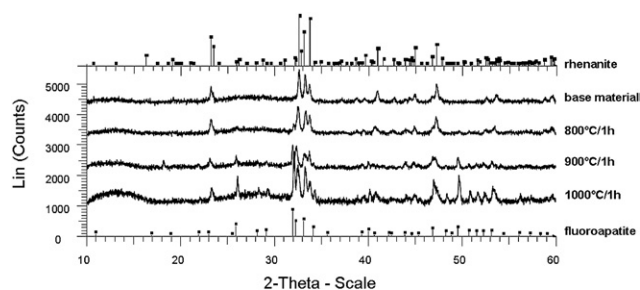

Fig. 1 XRD diagrams of glass and glass-ceramics of composition A. Rhenanite and fluoroapatite crystal phases were analyzed.
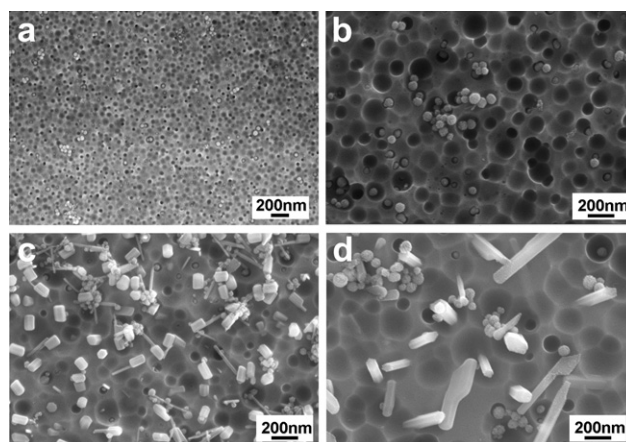

Fig. 2 Microstructures of base glass and glass-ceramics A after etching with aqueous 3% HF for 10 s (SEM). a) The base material shows holes representing the areas of precipitated rhenanite crystals. b) Glass-ceramic after heat treatment of 800 °C for 1 h. Rhenanite is the main crystal phase. c, d) Glass-ceramics after 900 °C for 1 h (c) and 1000 °C for 1 h (d) annealing. Fluoroapatite crystals grow and show needle-like morphology at 1000 °C.

100–200 nm in samples etched with H_3PO_4. The chemical nature of the glassy matrix and the nature of the crystals have to be taken into account in the discussion of the etching reaction and the micrographs. Aqueous HF etches the silica-rich glassy phase, while liquid H_3PO_4 etches the phosphate crystal phase. Therefore, the holes seen in Fig. 2b represent the size of the crystals and show the spherical morphology of the nanocrystals which have a diameter of approximately 100–200 nm. The crystals are isolated in the glassy matrix and do not touch each other. However, Fig. 2a shows a special phenomenon, namely that of preferred etching of the silica areas in the neighborhood of the ball-shaped crystals. Based on this finding, different chemical composition gradients are to be expected in the glassy matrix.

The microstructure of the samples heat treated at temperatures up to 800 °C remains nearly the same in comparison to the quenched base glass (Fig. 2b). In contrast, the microstructure of the sample heat treated at 900 °C (Fig. 2c) shows two other crystal phases of needle-like morphology in addition to the nano-sized rhenanite crystals. Both needle types represent fluoroapatite. The crystal type with dimensions of 200 nm × 20 nm is not found in samples annealed at higher temperatures. The second type of fluoroapatite crystal (200 nm × 100 nm) shows the typical needle-like shape at 1000 °C (Fig. 2d). The image in Fig. 2d shows a number of significant details: the hexagonal cross section of the growing needle-like fluoroapatite, randomly precipitated fluoroapatite without textures and the remaining rhenanite crystals.

3.2.3. Transmission electron microscopy analyses. In addition to the SEM investigations, further electron microscopy studies of glass-ceramic A heat treated at 1000 °C for 1 h were performed to characterize and to understand the microstructure formation as well as the distribution of the crystalline phases more comprehensively. Typical results of transmission electron microscopy (TEM) and scanning transmission electron microscopy (STEM) investigations are shown in Fig. 3 and 4, respectively. There are two different types of precipitates, namely needles (diameter
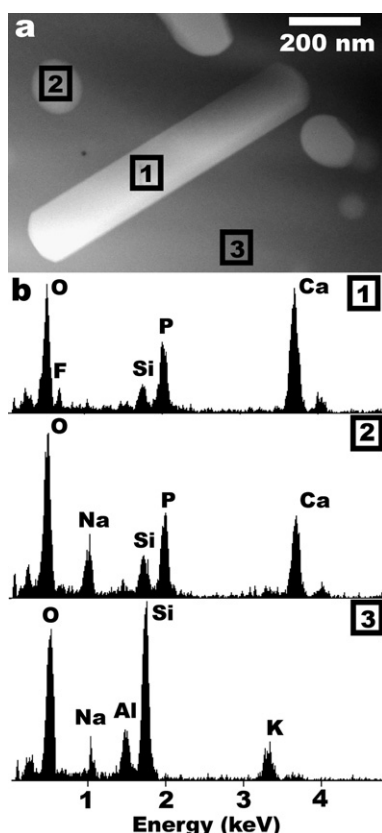
Fig. 3 Glass-ceramic obtained from the base glass A by heat treatment at 1000 °C. (a) HAADF-STEM image shows the presence of needle-like and almost round crystals; both appearing with bright contrast. (b) EDX spectra obtained at the areas outlined in (a), which show that the needles are fluoroapatite, $Ca_5(PO_4)_3F$ (area 1), and the round particles are rhenanite, $NaCaPO_4$ (area 2), while the glass matrix contains Na, Al, Si and K oxides (area 3).
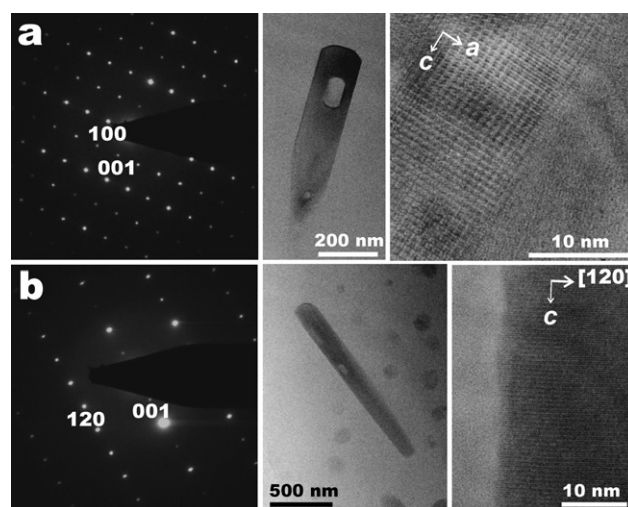

Fig. 4 Glass-ceramic obtained from the base glass A by heat treatment at 1000 °C. Selected area electron diffraction (SAED) patterns, TEM and HRTEM images of fluoroapatite crystals (dark contrast) oriented along (a) [010] and (b) [2$\bar{1}$0], respectively. In the SAED patterns (left side), two indices are given below the corresponding reflections. The HRTEM images (right side) demonstrate that the growth of the fluoroapatite crystals occurs along the crystallographic c axis. In the TEM image (b) (center), rhenanite (round particles) are present besides the approximately 1 μm long fluoroapatite crystal.

100–200 nm, length up to 1 μm) and round particles (diameter about 100 nm). The latter are actually spherical, as is evident from the SEM investigations mentioned above. Although the precipitated crystals occasionally overlap in some images, which is certainly due to the projection, they are isolated in most cases and randomly distributed in the glass matrix. This observation indicates that apatite needles and rhenanite spheres grow independently from each other.

In the STEM image (Fig. 3a) recorded with a HAADF detector, the different types of crystals appear with bright contrast in the dark glass matrix. EDXS analyses of the needle-like crystals (Fig. 3, area 1) reveal the presence of Ca, P, O and F corresponding to fluoroapatite. The presence of fluoroapatite is confirmed by the results of electron diffraction and HRTEM investigations on such needles. Typical SAED patterns (Fig. 4, left) show rectangular arrays of reflections. The distance in one direction in both patterns is approximately 0.69 nm, which is equivalent to the length of the crystallographic c axis of hexagonal fluoro-apatite ($P6_3/m$, $a = 0.9367$, $c = 0.6884$ nm).[20] In the perpendicular direction, values of approximately 0.805 nm (corresponds to the a axis of fluoroapatite) and approximately 0.31 nm (corresponds to d_{120}), respectively, were found. The SAED patterns were recorded from the fluoroapatite needles present in the TEM

images (center of Fig. 4). The HRTEM investigation of these needles (Fig. 4, right) reveals defect-free structures that are coherently embedded in the surrounding glass matrix. Consequently, homogeneous and unimpeded growth of the fluoro-apatite crystals has occurred in conjunction with a continuous transfer of the ions necessary for the formation of fluoroapatite from the glass to the crystal. In accordance with the SAED results, a repeat distance of approximately 0.69 nm in the direction of the needle axis appears in the HRTEM images. Obviously, the c axis represents the direction of crystal growth.

In the EDX spectrum of a spherical particle (Fig. 3, area 2), Ca, Na, P, and O are found, corresponding to rhenanite ($NaCaPO_4$). The glass matrix comprises K, Si, Al, Na, and O (Fig. 3, area 3) with Si being the main constituent. It is interesting to note that neither P nor F could be detected in the glass. Apparently, the amount of these elements present in the base glass A is used up to form rhenanite and fluoroapatite. Since the amounts of these elements, in particular that of F, were already rather small in the base glass A, it cannot be excluded that residuals of P and F are present in the glass (see NMR results in section 2.2.4). However, these traces would be below the detection limits of the EDXS method. Because fluoroapatite and rhenanite crystals are completely embedded in the glass matrix, the signal of Si also appears with considerable intensity in the spectra obtained at the sites of the precipitates (Fig. 3, areas 1 and 2).

The results of these electron microscopy investigations agree with the findings of the XRD studies (see section 2.2.1) that reveal the presence of crystalline rhenanite and fluoroapatite in ceramics obtained from the base glass A at temperatures above 900 °C.

3.2.4 NMR studies. Fig. 5a summarizes the ^{19}F NMR experiments conducted on glass A and its annealing products. All the
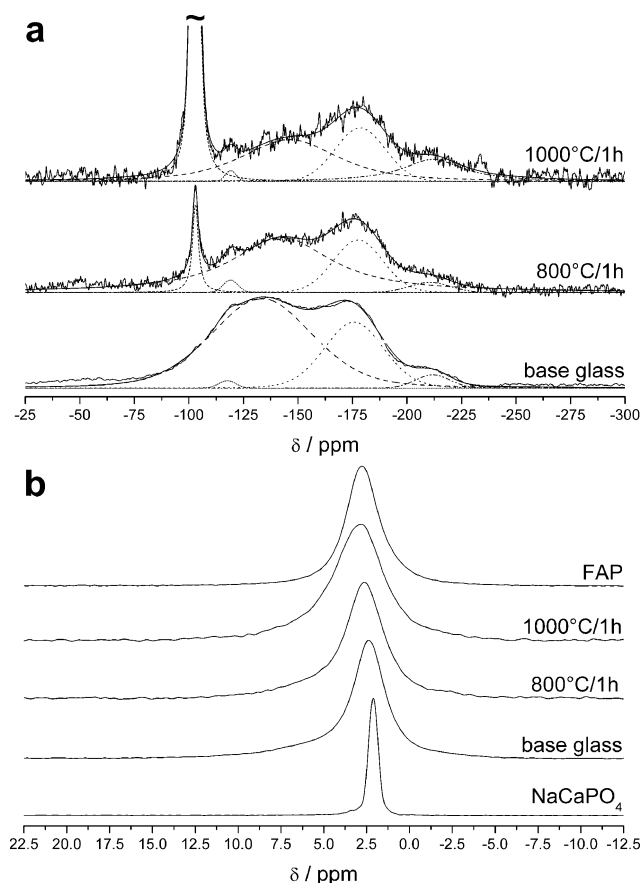
1322 | *J. Mater. Chem.*, 2008, **18**, 1318–1332

This journal is © The Royal Society of Chemistry 2008

results are summarized in Table 4. The ^{19}F MAS-NMR spectrum of the base glass reveals that all of the fluorine is in the amorphous state. Four signal contributions can be discerned, with resonance centers near −118, −130, −175, and −210 ppm, respectively. Based on previous ^{19}F{^{31}P} and ^{19}F{^{27}Al} double resonance studies done on similar compositions, the −118 and −130 ppm peaks can been assigned to fluoride in a Ca/P-dominated environment, while the −175 ppm peak is attributable to fluoride coordinated to aluminium; both fluorine species are most likely in separate phases. Based on its chemical shift, we can further attribute the −210 ppm resonance to fluoride ions in a Na-dominated environment. After sample annealing at 800 °C, the ^{19}F NMR spectrum reveals the formation of a small amount (corresponding to approximately 10% of the fluoride present) of fluoroapatite (peak near −104 ppm). While annealing the sample at 1000 °C converts a significant amount of the fluoride present into fluoroapatite, the majority of it (64%) still remains in the glassy state. This result, which differs from the conclusion drawn from the TEM data, is not surprising, as (1) the F/P$_2$O$_5$ ratio of the batch composition is higher than the corresponding ratio in FAP, and (2) a significant fraction of phosphorus is present as NaCaPO$_4$ (see below). Therefore, a substantial amount of fluoride present in the sample cannot be bound in the form of FAP and remains in the glassy state. As Fig. 5a and Table 4 indicate, the chemical environments of the Al- and Na-bound fluoride species (spectral components near −175 and −210 ppm) present in the residual glassy phase are not affected by the annealing process. In contrast, the spectral component near −130 ppm is significantly broadened and reduced in intensity with increasing annealing temperature, indicating that fluoride species from this glassy phase are the source of the FAP formation. The spectroscopic changes observed for this component most likely reflect the change in composition of the microphase containing this part of the fluorine inventory

Fig. 5 (a) ^{19}F MAS-NMR results on glassy and annealed samples of series A. The dotted and dashed curves indicate the individual contributions from peak deconvolution of the spectrum into three Gaussian lineshape components. (b) ^{31}P MAS-NMR results on glassy and annealed samples of series A and the model compounds FAP and NaCaPO$_4$.

Table 4 ^{19}F and ^{31}P MAS-NMR chemical shifts δ_{iso} (±0.2 ppm), full width at half maximum: fwhm (±0.2 ppm), populations of the different phases P (±5 %), and normalized difference signals $(S_0 - S)/S_0$ measured for a fixed dipolar evolution time in ^{31}P{^{19}F}, ^{31}P{^{23}Na} and ^{19}F{^{31}P} REDOR as well as ^{19}F{^{23}Na} TRAPDOR experiments on base glass A and its annealing products

	^{19}F-MAS			^{19}F{^{31}P} REDOR $(S_0 - S)/S_0$, $T_D = 1.5$ ms	^{19}F{^{23}Na} TRAPDOR $(S_0 - S)/S_0$, $T_D = 0.7$ ms	^{31}P-MAS			^{31}P{^{19}F} REDOR $(S_0 - S)/S_0$, $T_D = 1.0$ ms	^{31}P{^{23}Na} REDOR $(S_0 - S)/S_0$, $T_D = 1.0$ ms
Sample	δ_{iso} (ppm)	fwhm (ppm)	P (%)			δ_{iso} (ppm)	fwhm (ppm)	P (%)		
NaCaPO$_4$						2.1	0.7	100		0.49
Base glass A	−212	19	3	0.04	0.67	2.4	2.1	78	0.01	0.51
	−176	32	29	0.00	0.43	4.5	7.4	22	0.26	0.10
	−133	55	68	0.14	0.42					
	−118	9	1	1.00	0.00					
800 °C, 1 h	−211	32	9	0.01	0.72	2.6	2.4	73	0.04	0.50
	−178	26	22	0.00	0.41	3.8	7.0	27	0.30	0.30
	−140	69	62	0.17	0.45					
	−119	8	1	1.00	0.00					
	−103	3	7	0.53	0.00					
1000 °C, 1 h	−212	33	12			2.9	3.2	85	0.14	0.39
	−179	27	17			4.5	6.0	15	0.38	0.01
	−146	57	35							
	−103	4	36							
FAP	−103	5	100	0.77		2.7	2.3	100	0.62	

as the crystallization of FAP proceeds. Fig. 5b shows the ^{31}P MAS-NMR results. The spectrum of the base glass consists of a broad signal centered near 4.5 ppm and a sharp resonance near 2.4 ppm. The latter confirms that a substantial fraction of the phosphorus species (about 78%) in this "base glass" is already in the crystalline state. The chemical shift of 2.4 ppm lies between the values measured in the reference compounds NaCaPO$_4$ (2.1 ppm) and apatite (2.7 ppm). When samples are annealed at 800 and 1000 °C, the sharp signal broadens somewhat and gradually shifts towards the resonance measured in fluoroapatite, while a substantial fraction of phosphorus (around 15% in the sample annealed at 1000 °C) still remains in the glassy state. Since the chemical shifts of these two reference compounds are too close to each other, their individual contributions to the signal cannot be quantified safely as only one composite signal is observable. As the studies have shown that the chemical shifts attributed to these compounds formed in different ceramics are subject to substantial sample-to-sample variations, it would not be safe to deduce approximate ratios for them based on the average chemical shift measured. Nevertheless, the chemical shift observed in Fig. 5b certainly suggests that the fluoroapatite-to-rhenanite ratio increases with increasing annealing temperature. More quantitative information

regarding the phase composition comes from the ^{31}P{^{19}F} and ^{31}P{^{23}Na} REDOR experiments shown in Fig. 6. As the annealing temperature increases, the extent of the ^{31}P–^{23}Na dipolar dephasing gradually diminishes, while that of the ^{31}P–^{19}F dipolar dephasing increases. Most significantly, however, the ^{31}P{^{23}Na} REDOR signal of the sample annealed at 1000 °C indicates that a substantial fraction of the crystallized phosphate species is still present in the rhenanite phase (NaCaPO$_4$), even though this phase cannot be clearly detected by XRD or the ^{31}P chemical shift any longer. We can estimate their corresponding fractions based on the magnitude of the ^{31}P{^{19}F} and ^{31}P{^{23}Na} REDOR effects associated with the sharp peak in relation to those observed in the pure reference compounds. In nicely consistent results, the ^{31}P{^{19}F} REDOR data show that 20% of the phosphorus atoms are present in the form of fluoroapatite, while the ^{31}P{^{23}Na} REDOR results indicate that 80% of the phosphorus atoms are present in the form of rhenanite. All these conclusions are re-inforced by the DTA data presented in Fig. 7a, revealing the characteristic endothermal signal of the NaCaPO$_4$ first-order solid–solid phase transition (Fig. 7b) in all of the annealing products. This result clearly reveals that rhenanite is not a precursor phase to FAP, but rather that the crystallization of both phases occurs in parallel processes. Based on all these
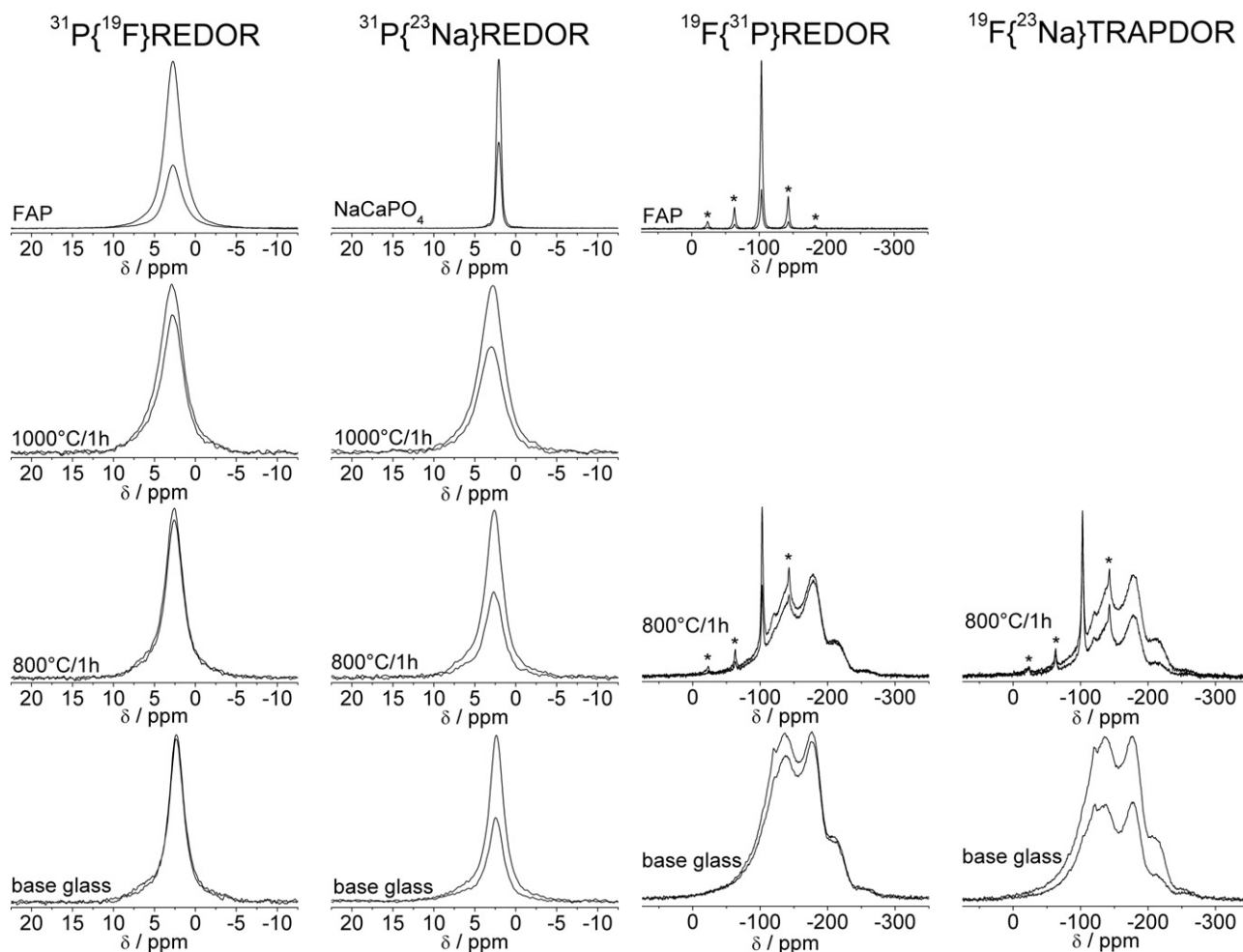

Fig. 6 ^{31}P{^{19}F} REDOR, ^{31}P{^{23}Na} REDOR, ^{19}F{^{31}P} REDOR and ^{19}F{^{23}Na} TRAPDOR NMR results on samples of series A and the model compounds FAP and NaCaPO$_4$. In each plot the smaller trace is the spectrum obtained with dipolar recoupling applied.
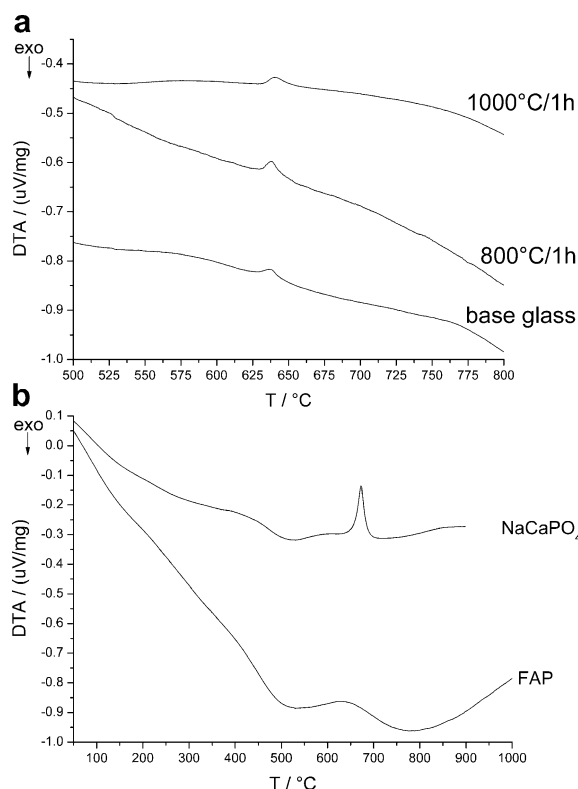
Fig. 7 (a) Differential thermal analysis results obtained on samples of series A. The individual traces have been offset for clarity. (b) Differential thermal analysis results obtained on model compounds FAP and NaCaPO$_4$. The individual traces have been offset for clarity.

Fig. 8 XRD patterns of base material and glass-ceramics with composition B. The precipitation of fluoroapatite is evident after heat treatment at 800 °C for 1 h.

Fig. 9 SEM images of base glass and glass-ceramic of composition B. SEM etched samples (3% HF, 10 s). The base glass (a) shows holes, representing the precipitation of the primary crystal phase. Needle-like fluoroapatite was growing at 1000 °C (b).

results, the spectral component seen near −130 ppm in the ^{19}F NMR spectra represents the fluoride environment in the glass component from which the fluoroapatite crystals grow upon annealing above 800 °C. The phosphorus environment in this amorphous state is characterized by the broad component discernable in the ^{31}P NMR spectra near 4–5 ppm. Unfortunately, its poor spectroscopic differentiation from the sharp component and its overall low intensity lead to low precision in the ^{31}P{^{19}F} and ^{31}P{^{23}Na} double resonance characterization, thereby precluding a more detailed quantitative characterization. Nevertheless, on a qualitative basis these results suggest that the P atoms exhibit spatial proximity with both sodium and fluoride ions.

3.3. Phase formation in glass and glass-ceramic B

3.3.1. Crystal phase precipitation. The rapidly quenched glass B is transparent and, in comparison to glass A, does not show any opacity or precipitation. Surprisingly, however, the XRD investigation of Fig. 8 reveals two weak diffraction peaks, indicating the formation of a crystal phase in the base glass. The diffraction peaks do not correspond exactly to fluoroapatite. As discussed further below in connection with the TEM and NMR results, this phase might be characterized as a disordered fluoroapatite. These spherical crystals measure less than 100 nm and the crystals are isolated from each other. Therefore, the material is still transparent.

The crystal phase formation of fluoroapatite starts within the process of thermal treatment of the base glass (with the
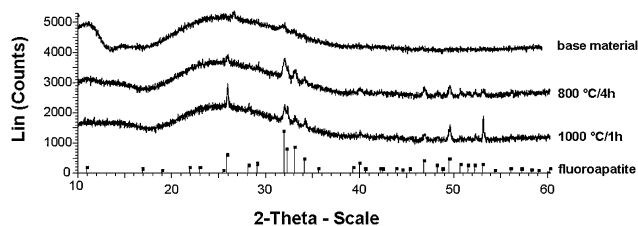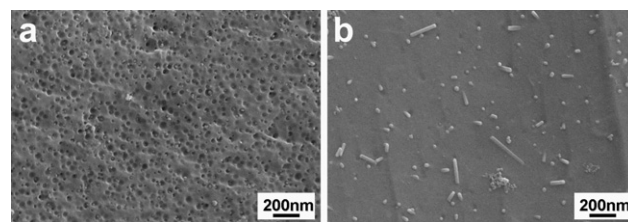
"disordered crystal phase") at 800 °C for 1 h. It is growing after four hours of heat treatment and continues up to 1000 °C.

3.3.2. Microstructure formation. The microstructure of the base glass with the primary crystal phase is shown in Fig. 9a. The microstructure of the glass-ceramic heat treated at 800 °C (not illustrated) is not significantly changed. However, the phase content is different. The precipitation of fluoroapatite started on a nanometer scale. The location of the fluoroapatite crystals in comparison to the analyzed primary crystal phase could not be determined by SEM.

Needle-like fluoroapatite crystal growth starts at 950 °C. At 1000 °C the crystals measure approximately 200 nm to 500 nm (Fig. 9b). The crystals grow randomly oriented in the glassy matrix and no preferred texture is visible. Because of the different chemical composition of glass B in comparison to glass A, the crystal content of fluoroapatite is much lower in glass B than in glass A.

3.3.3. Electron microscopy analyses of glass-ceramic B. The formation of needle-like fluoroapatite in the glass-ceramic obtained from base glass B starts at temperatures above 950 °C. STEM images after heat treatment at 1000°C for 1 h (Fig. 10a, b) show that the morphology and the direction of crystal growth are analogous to those of the fluoroapatite crystals observed in sample A. EDX spectra show that the needles contain Ca, P, O and F and thus are indeed fluoroapatite (Fig. 10c, area 1). The strong peak of Si arises from the Si-rich glass surrounding the needles. EDX spectra of the glass matrix show pronounced peaks of Si, Al, O and a small one of K (Fig. 10c, area 2). Remarkably, the glass matrix is free from the elements of Ca, P, O and F within the detection limits, suggesting that they are completely consumed during the formation of fluoroapatite (however see NMR results, below).
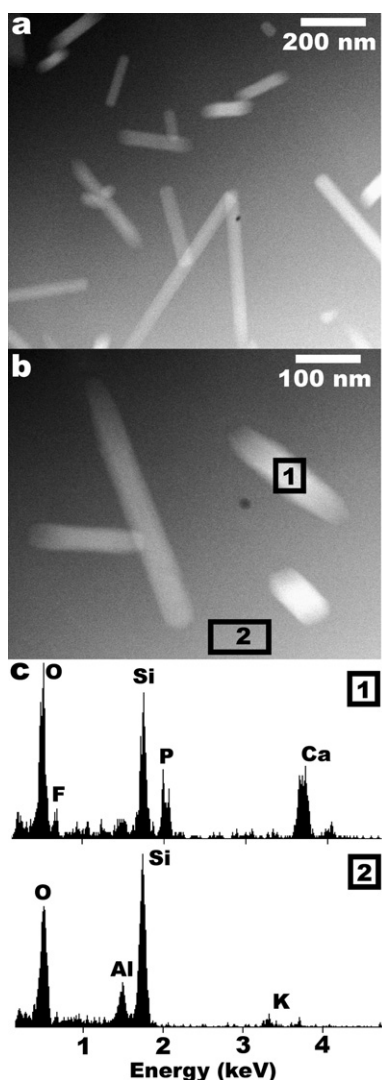
Fig. 10 Glass-ceramic obtained from the base glass B through heat treatment at 1000 °C. (a,b) HAADF-STEM images showing the presence of needle-like crystals (bright contrast) at random orientation. (c) EDX spectra obtained at the corresponding areas in (b), which show that the needles are fluoroapatite ($Ca_5(PO_4)_3F$) (area 1), while the matrix contains mainly Al and Si oxide and a small amount of K (area 2).

The diameter of the needles is in the range 50–100 nm, while their length is up to 0.5 μm (Fig. 10a, b). Therefore, their size on average is a bit smaller than that observed for the needles in sample A (Fig. 3, 4). It has to be noted, however, that the needles are randomly oriented in the glass matrix. Therefore, their maximum length can be observed only if a needle is by chance oriented along the needle axis. Cutting the needles in an arbitrary direction during TEM specimen preparation, leads to shorter fragments observed in projection. The extreme case occurs if a needle is oriented perpendicularly to the cutting plane: then, the cross-section can be investigated.[16]

Annular dark field (ADF) STEM images of the primary crystal phase (Fig. 11) reveal that round particles are embedded inside the base glass B. Their diameter is in the range of 10–20 nm. Since their outline is always round, it can safely be postulated that their morphology is spherical. Further characterization by
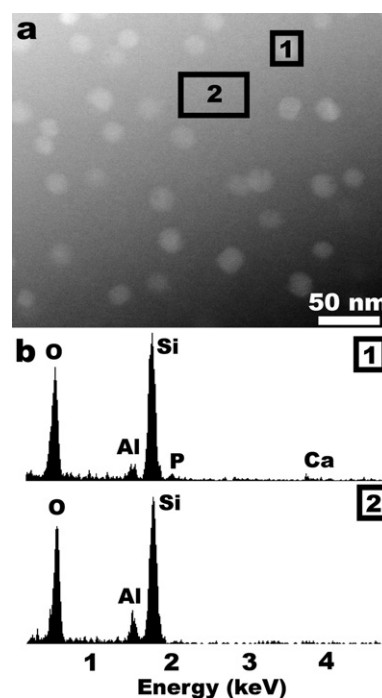

Fig. 11 (a) ADF-STEM image of base glass B. Presumably spherical particles with diameters in the range of 10–20 nm appear as bright round patches. (b) EDX spectra obtained at the corresponding areas in (a). The EDX spectrum of a segregated particle (area 1) show small amounts of Ca and P besides the large peaks of Si and Al of the glassy matrix (area 2).

electron microscopy means is difficult since these particles are very sensitive to the electron beam and rapidly decompose. In very thin specimen regions, this leads to a hole in the sample. In rare cases, enough X-rays could be collected before decomposition to detect small amounts of Ca and P, besides the large peaks of Al and Si present in the glass matrix. This observation indicates that these spherical inclusions indeed correspond to the sought primary phase related to fluoroapatite as detected by the XRD and NMR investigations (see above).

3.3.4 NMR studies. Fig. 12a summarizes the ^{19}F NMR results of the base glass and the sample annealed at 1000 °C for 1 h; results from the data analysis are summarized in Table 5. The spectrum of the base glass looks very much like that of sample A, indicating the presence of the same multiple fluoride environments. In addition, a very small fraction (approximately 2% of the fluoride present) of crystalline fluoroapatite can be detected. After annealing at 1000 °C, the amount of apatite has increased only very little, while most of the fluoride is still found in the glassy state. This observation is not unexpected, as the F/P ratio in this sample is significantly in excess of that required for stoichiometric apatite formation. Similar to the situation in glass system A, annealing leaves the spectral component near −175 ppm (Al-bound F) unaffected, whereas the spectral parameters of the component near −130 ppm are significantly altered, resulting in severe broadening and reduction in overall intensity. Fig. 12b shows the results from the ^{31}P MAS-NMR studies. While in the base glass the large majority of phosphorus is still in the glassy state, a small fraction of it seems to have crystallized, giving rise to the sharp signal near 3.2 ppm.
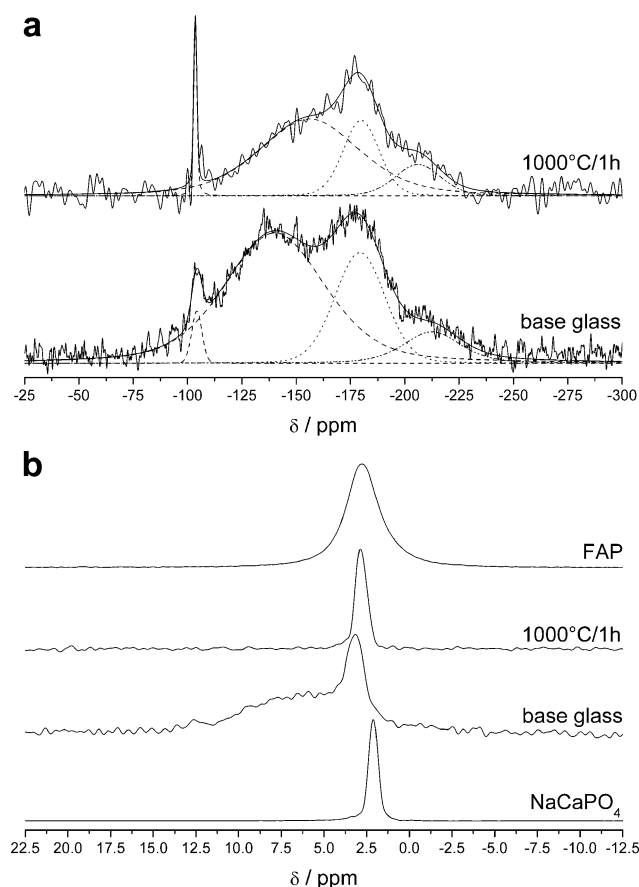
Fig. 12 (a) ^{19}F MAS-NMR spectra of the base glass of series B and the sample annealed at 1000 °C. The dotted and dashed curves indicate the individual contributions from peak deconvolution of the spectrum into three Gaussian lineshape components. (b) ^{31}P MAS-NMR spectra of the base glass B, the sample annealed at 1000 °C and the model compounds FAP and NaCaPO$_4$.

The chemical shift difference of this peak from that measured in fluoroapatite is outside the experimental error. Thus, we can conclude that the species formed here may be structurally similar, but is not identical to regular fluoroapatite. Further

annealing (1000 °C for 1 h) causes the large majority of phosphorus to crystallize. In addition, the sharp ^{31}P resonance near 2.8 ppm signifies the formation of bulk fluoroapatite. The double resonance studies summarized in Fig. 13 strongly reinforce these conclusions. The ^{31}P{^{19}F} REDOR results indicate a strong phosphorus-fluoride interaction in the base glass, which is already comparable to that measured in fluoroapatite. Given the low concentrations of both elements, this result clearly indicates the phase separated character of this glass, illustrating that the local P environment in it closely resembles that of fluoroapatite. The crystalline phases formed both in the base glass and in the sample annealed at 1000 °C show comparable ^{31}P/^{19}F interaction strengths, which are indistinguishable from those measured in crystalline fluoroapatite. At the same time, the ^{31}P{^{23}Na} REDOR data reveal no proximity between phosphorus and sodium, indicating the complete absence of rhenanite or of any type of rhenanite-like glassy precursor environment in these samples. This situation is different from that in the glass system A, where a substantial P/Na interaction can be detected. Furthermore, Fig. 13 includes ^{31}P{^{27}Al} TRAPDOR data; the absence of any observable dipolar interaction between these nuclei indicates no spatial proximity between P and Al, consistent with the phase separated character of this glass. Based on the very weak ^{31}P–^{23}Na and ^{31}P–^{27}Al dipolar interaction in the base glass B, it appears that in this material the large majority of the phosphorus inventory is already segregated into amorphous domains with fluoroapatite-like compositions. As such, the ^{31}P and ^{19}F NMR data obtained on this precursor glass within the present study serve to provide valuable characterization data on these amorphous fluoroapatite domains. In addition the precursor glass already contains a small amount of a crystalline fluoroapatite-like phase. However, this phase may be subject to some degree of structural or compositional disorder, as suggested by the broad ^{19}F NMR spectrum and by the fact that the ^{31}P chemical shift (3.2 ppm) deviates from the usual value (2.8 ppm). In fact, chemical shift variations of this magnitude have been found previously for other apatite phases crystallized during the heat treatment of other ceramic sample formulations.[21] Finally, both the NMR data and the DTA results (Fig. 14) prove the absence of any NaCaPO$_4$ in the samples of glass ceramic system B.

Table 5 ^{19}F and ^{31}P MAS-NMR chemical shifts δ_{iso} (±0.2 ppm), full width at half maximum: fwhm (±0.2 ppm), populations of the different phases P (±5 %), and normalized difference signals $(S_0 - S)/S_0$ measured for a fixed dipolar evolution time in ^{31}P{^{19}F} and ^{31}P{^{23}Na} REDOR experiments on base glass B and its annealing products

Sample	^{19}F-MAS			^{31}P-MAS			^{31}P{^{19}F} REDOR $(S_0 - S)/S_0$, $T_D = 1.6$ ms	^{31}P{^{23}Na} REDOR $(S_0 - S)/S_0$, $T_D = 1.0$ ms
	δ_{iso} (ppm)	fwhm (ppm)	P (%)	δ_{iso} (ppm)	fwhm (ppm)	P (%)		
NaCaPO$_4$				2.1	0.7	100		0.49
Base glass B	−213	31	9	3.2	1.2	28	0.80	0.07
	−179	27	25	6.5	7.5	72	0.81	0.21
	−140	55	64					
	−104	6	2					
1000 °C, 1 h	−206	25	11	2.8	0.8	100	0.83	0.00
	−180	20	21					
	−156	54	63					
	−104	2	5					
FAP	−103	5	100	2.7	2.3	100	0.82	

$^{31}P\{^{19}F\}REDOR$ $^{31}P\{^{23}Na\}REDOR$ $^{31}P\{^{27}Al\}TRAPDOR$
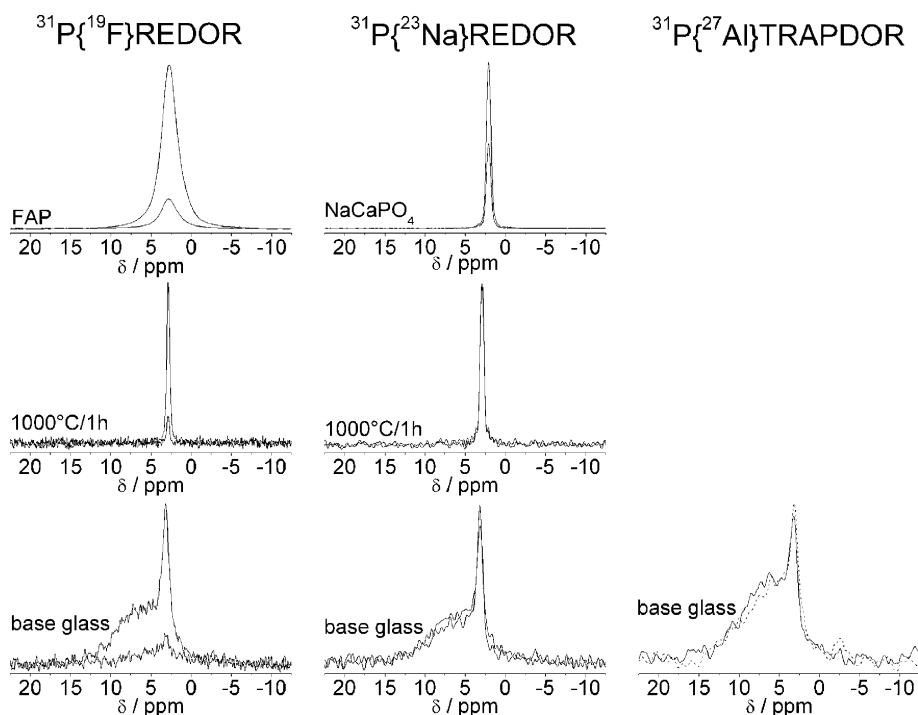
Fig. 13 $^{31}P\{^{19}F\}$ REDOR (left), $^{31}P\{^{23}Na\}$ REDOR (middle) and $^{31}P\{^{27}Al\}$ TRAPDOR NMR results on samples of series B and the model compounds FAP and NaCaPO$_4$. In each plot the smaller trace is the spectrum obtained with dipolar recoupling applied.
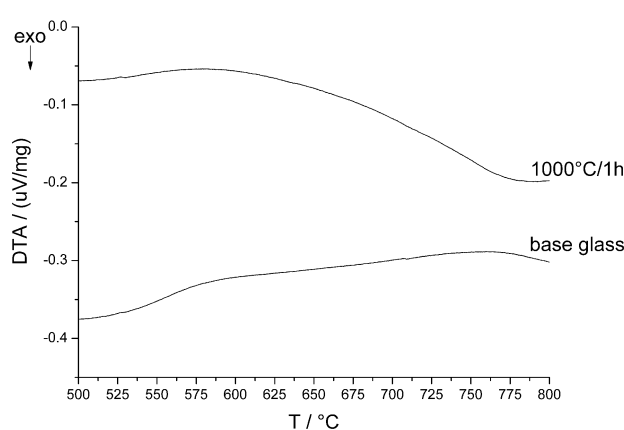

Fig. 14 Differential thermal analysis results obtained on samples of series B. The individual traces have been offset for clarity.

Fig. 15 X-Ray diffraction diagrams of glass-ceramic C.

3.4. Phase formation and crystallization in reference glass system C

3.4.1. X-Ray diffraction studies and thermal analysis characterization.
Fig. 15 presents X-ray diffraction data, which clearly reveal the exclusive formation of rhenanite, NaCaPO$_4$ in all of the samples heat treated. No FAP is detectable. These results are supported by the DTA data presented in Fig. 16 showing the characteristic endotherm peak of rhenanite phase transformation. However, no rhenanite crystallization takes place on the base glass under DTA conditions.

3.4.2. NMR Studies.
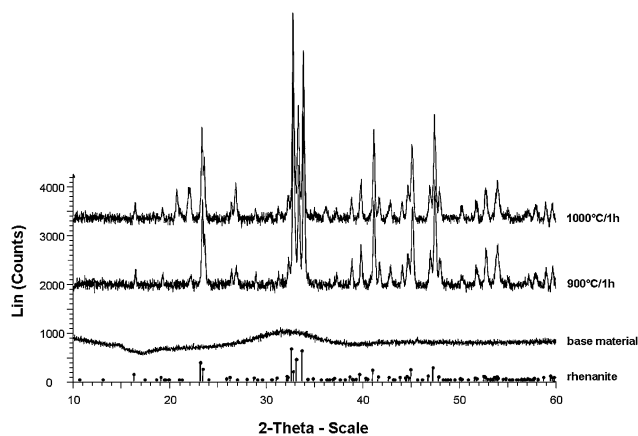Fig. 17–19 summarize the ^{19}F MAS, the ^{31}P MAS, and the double resonance studies of glass system C.

Table 6 summarizes the quantitative deconvolution results of these spectra. While the ^{19}F spectra again reveal three major fluoride environments (as in samples A and B), the chemical shifts associated with these components are somewhat different: the three major signal components are found near -140, -170 and -218 ppm, respectively. Based on the double resonance NMR results discussed below, we assign the broad signal component near -140 ppm to a fluorine species in a Ca/P dominated environment. There is a possibility that the resonance near -170 ppm could be attributed to fluorine species interacting with the silicate component (Si-bound species), while the signal near -218 ppm is again assigned to F in a sodium-dominated environment. In contrast to the situation with the other two glasses, no fluoroapatite is formed upon sample annealing at 1000 °C for
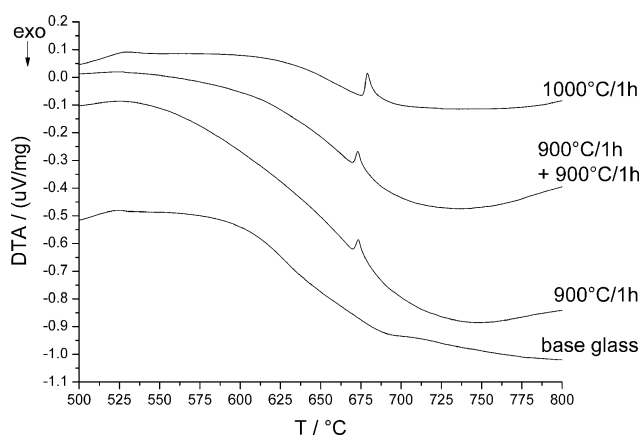
Fig. 16 Differential thermal analysis results obtained on samples of series C. The individual traces have been offset for clarity.
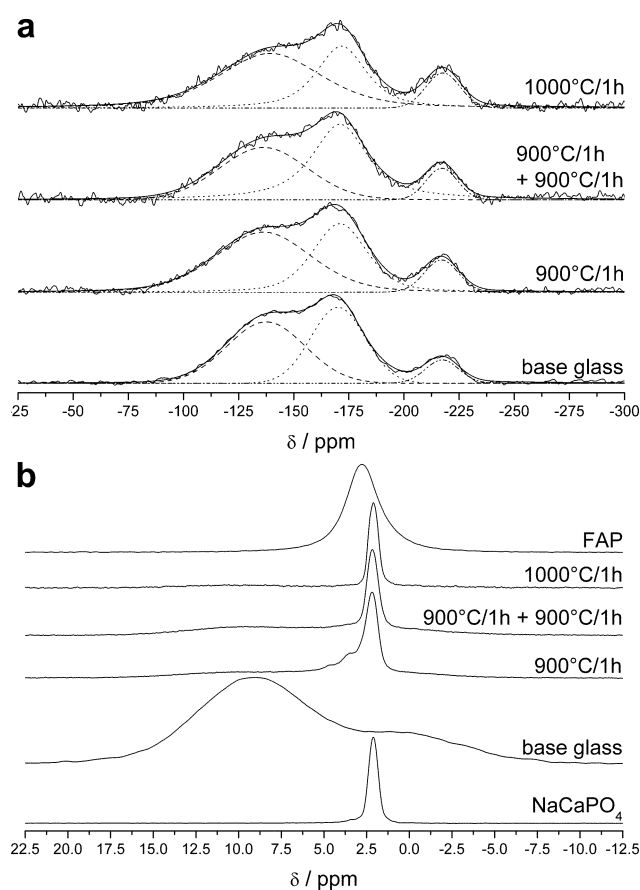

Fig. 17 (a) ^{19}F MAS-NMR spectra of the series C samples. The dotted and dashed curves indicate the individual contributions from peak deconvolution of the spectrum into three Gaussian lineshape components. (b) ^{31}P MAS-NMR spectra of the series C samples and model compounds FAP and NaCaPO$_4$.

Fig. 18 ^{19}F\{^{31}P\} REDOR (left) and ^{19}F\{^{23}Na\} TRAPDOR NMR results on samples of series C and the model compound FAP. In each plot the smaller trace is the spectrum obtained with dipolar recoupling applied.

fluoride species present comparable ^{19}F–^{31}P dipolar interaction strengths. This result is in agreement with a statistical distribution of the phosphate and fluoride anions in the base glass, suggesting that this material is chemically homogeneous and does not contain different fluoride species in different microphases. Nevertheless, the ^{31}P\{^{23}Na\} TRAPDOR data of the base glass indicate an interesting differentiation with respect to the interaction with the cations present: the peak near −140 ppm reflects a fluoride species in an environment that is essentially devoid of sodium ions, whereas the other two species present comparable ^{19}F/^{23}Na dipolar interaction strengths.

For all the three of these species, the ^{19}F/^{31}P dipole–dipole interaction is found to be substantially weakened in the sample annealed at 900 °C for 1 h. This result is immediately understandable as the crystallization of NaCaPO$_4$ results in a dilution of the residual glassy phase with respect to the phosphate species; as Fig. 18 shows, this process can be nicely monitored by double resonance NMR.

In contrast, the NaCaPO$_4$ crystallization produces no significant change in the overall ^{19}F/^{23}Na dipolar interaction strength as the amount of sodium removed from the glassy phase by NaCaPO$_4$ crystallization is insignificant in relation to the overall sodium content of the glass. Fig. 17b and 18 show ^{31}P single and double resonance NMR results obtained on the base glass and materials with different annealing stages. The base glass shows two ^{31}P resonances at 9.2 and 0.0 ppm, which can be assigned, on the basis of their chemical shifts, to Q$^{(0)}$ and Q$^{(1)}$ species, respectively. The double resonance NMR results of this material (Fig. 18, bottom) reveal that both species show no differentiation

1 h. Rather, the entire fluoride inventory is left in the amorphous state. The fluorine environments in this glass and their changes upon NaCaPO$_4$ crystallization are further characterized by the ^{19}F\{^{31}P\} REDOR and ^{19}F\{^{23}Na\} TRAPDOR studies summarized in Fig. 18. In the base glass, all of the three discernible

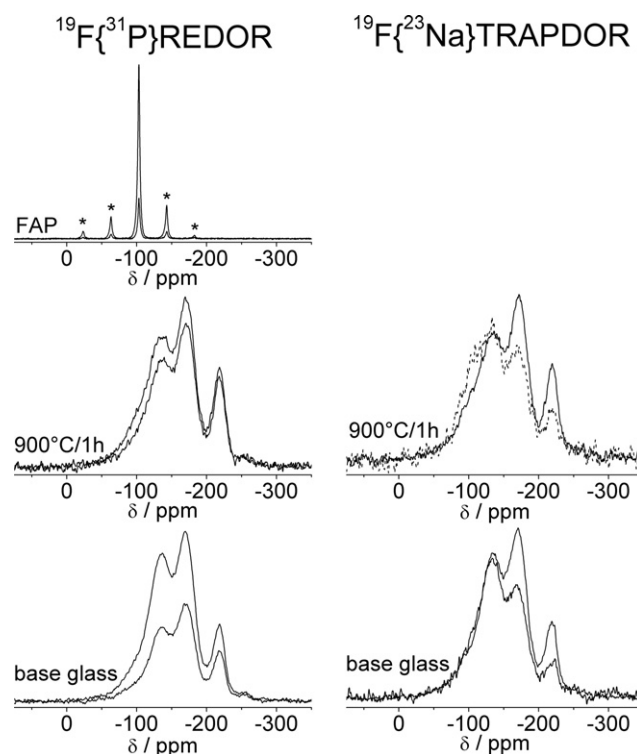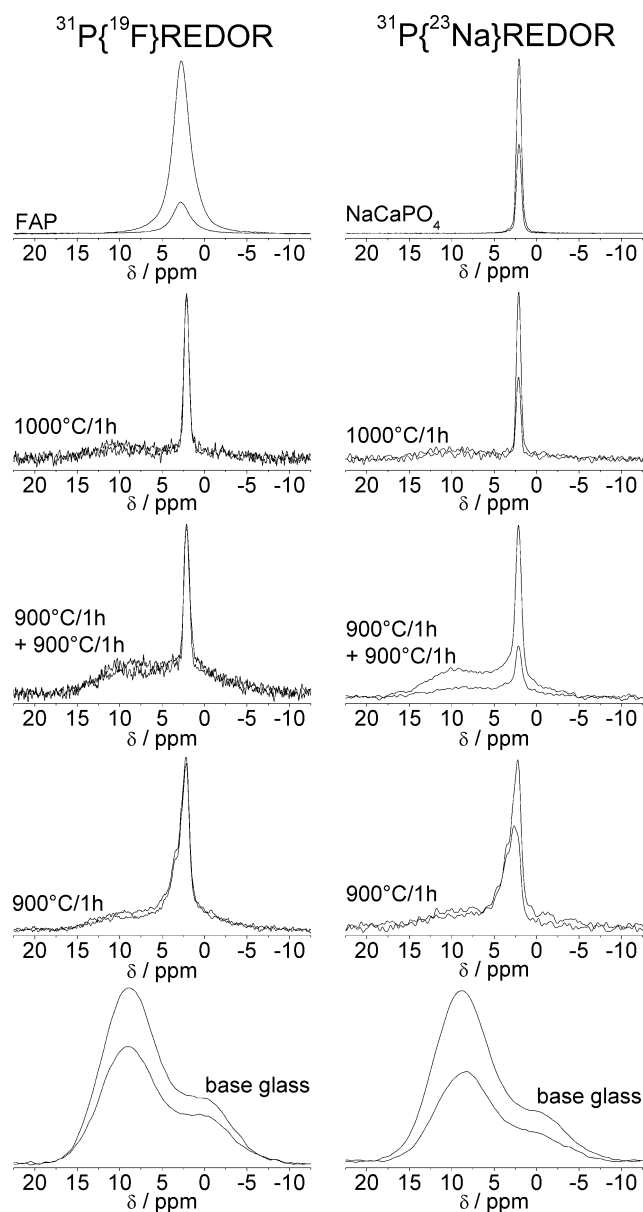**Fig. 19** $^{31}P\{^{19}F\}$ REDOR (left) and $^{31}P\{^{23}Na\}$ REDOR NMR results on samples of series C and the model compounds FAP and $NaCaPO_4$. In each plot the smaller trace is the spectrum obtained with dipolar recoupling applied.

with respect to the strength of their interaction with either ^{19}F or ^{23}Na, in agreement with the homogeneous, non-phase separated character of the glassy material. The single and double resonance spectra show further that $NaCaPO_4$ is the main crystallization product and that this phase remains stable at all annealing stages. This is seen by the consistent absence of a $^{31}P\{^{19}F\}$ REDOR effect, and the presence of a strong $^{31}P\{^{23}Na\}$ REDOR effect of comparable magnitude to that observed in $NaCaPO_4$. Thus, the results obtained in this series of samples also illustrate the lack of reactivity associated with the rhenanite phase, as it clearly remains stable in the presence of fluoride species in the softened glass matrix. This result, too, argues against the idea that rhenanite represents a precursor to fluoroapatite in these ceramics.

Finally, Fig. 19 reveals all three annealed samples still contain significant amounts of phosphorus in the amorphous state (broad component near 10 ppm). Unfortunately, the poor spectroscopic resolution and low intensity of this spectral component produces large errors in the analysis of the double resonance data, rendering a more detailed discussion impossible.

4. Conclusions

From the results of the experimental studies on fluoroapatite glass-ceramic A and B and the discussion on the microstructure formation in the base glasses and the heat-treated samples, we can draw the following conclusions about the phase sequence and formation mechanisms of the main crystal phases.

a) Glass-ceramic A

Rhenanite ($NaCaPO_4$) is the primary crystal phase and is already formed during the cooling of the liquid melt. As was the case in the reference glass-ceramic C, the crystals grew in a spherical shape.[14,22] Rhenanite has an orthorhombic crystal lattice ($Pn21a$) in which $a = 2.0397$ nm, $b = 0.5412$ nm and $c = 0.9161$ nm.[23]

The crystal formation process of fluoroapatite begins at 800 °C. Up to a temperature of 1000 °C, the crystals grow in a needle-like shape. Fluoroapatite crystallizes in a hexagonal system with the lattice parameters of $a = 0.9367$ nm and $c = 0.6884$ nm.[20] In an earlier study, this growth process was characterized as Ostwald ripening.[24] TEM analyses were used to conduct a close examination of the microstructure formation in samples that had been heat treated at temperatures up to 1000 °C. The examination did not reveal any growth of fluoroapatite on rhenanite. As a result, previous assumptions that epitaxial interactions occur between rhenanite and fluoroapatite cannot be confirmed.[20,21,25,26,] Rather, on the basis of the detailed microstructural analysis and solid state NMR data we conclude that the processes involved in the formation of rhenanite and fluoroapatite are two parallel solid state chemical reactions that occur in the glass-ceramic fabrication process. $^{31}P\{^{23}Na\}$ and $^{31}P\{^{19}F\}$ solid state double resonance NMR techniques present a powerful tool for monitoring the formation of both crystalline materials in a quantitative manner.

b) Glass-ceramic B

As glass-ceramic B contains a smaller amount of Na_2O than glass-ceramic A, rhenanite is not formed as the primary crystal phase. However, it is interesting to note that despite the low concentration of CaO and P_2O_5 in glass-ceramic B, another crystal phase forms as the primary crystal phase during cooling of the liquid melt. These spherically shaped crystals have very uniform nanoscale dimensions with a diameter of approximately 20 nm. The X-ray diffraction investigations show that this crystal phase is not exactly fluoroapatite, as the main diffraction peaks of the [002] and [211] reflections are not completely attained. The [002] peak of fluoroapatite is at 25.86° (2θ) and the [211] diffraction peak is at 31.94° (2θ). The NMR data, however, suggest that this phase can be described as a structurally disordered fluoroapatite. Furthermore, based on the NMR results and the spherical morphology, clearly shown in the TEM analyses, we

Table 6 ^{19}F and ^{31}P MAS-NMR chemical shifts δ_{iso} (± 0.2 ppm), full width at half maximum: fwhm (± 0.2 ppm), populations of the different phases P (± 5 %), and normalized difference signals $(S_0 - S)/S_0$ measured for fixed dipolar evolution times in ^{31}P{^{19}F}, ^{19}F{^{31}P}, and ^{31}P{^{23}Na} REDOR and ^{19}F{^{23}Na} TRAPDOR experiments on base glass C and its annealing products

Sample	^{19}F-MAS δ_{iso} (ppm)	fwhm (ppm)	P (%)	^{19}F{^{31}P} REDOR $(S_0-S)/S_0$, $T_D=1.5$ ms	^{19}F{^{23}Na} TRAPDOR $(S_0-S)/S_0$, $T_D=0.7$ ms	^{31}P-MAS δ_{iso} (ppm)	fwhm (ppm)	P (%)	^{31}P{^{19}F} REDOR $(S_0-S)/S_0$, $T_D=1.6$ ms	^{31}P{^{23}Na} REDOR $(S_0-S)/S_0$ $T_D=1.0$ ms	$T_D=1.4$ ms
NaCaPO$_4$ ref.						2.1	0.7	100		0.49	
Base glass C	−217	18	8	0.31	0.60	0.0	7.9	25	0.27	0.41	
	−170	29	43	0.39	0.45	9.2	7.6	75	0.34	0.48	
	−138	42	49	0.50	0.03						
900 °C, 1 h	−217	18	10	0.06	0.54	2.2	0.8	34	0.01	0.46	0.45
	−171	29	37	0.08	0.36	3.2	1.5	13	0.05	0.00	0.00
	−136	51	53	0.18	−0.05	4.7	0.7	2	0.30	0.25	0.35
						3.2	8.9	31	0.21		0.66
						10.9	7.0	20	0.24		0.67
900 °C, 1 h +	−217	17	9			2.1	0.8	31	0.00		0.73
900 °C, 1 h	−171	30	50			2.5	7.7	45	0.30		0.64
	−136	47	41			10.1	6.8	24	0.23		0.64
1000 °C, 1 h	−218	18	10			2.1	0.7	61 (38)	0.00	0.51	
	−172	27	34			1.0	7.1	19 (32)	0.38	0.35	
	−139	55	56			10.4	7.0	20 (30)	0.40	0.35	
FAP ref.	−103	5	100	0.77		2.7	2.3	100	0.82		

conclude that amorphous phase separation processes promote the nucleation process for primary phase formation. As the glass-ceramic heat treatment temperature rises, this primary phase containing phosphate is converted into fluoroapatite through a solid state reaction and completely disintegrates. In contrast to rhenanite, it is not evident at higher temperatures in glass-ceramic A. Furthermore, the results show that fluoroapatite does not grow in needle-like form initially, but rather acquires its needle-like morphology at an advanced stage of growth. The crystals grow along the c axis, which is confirmed by HRTEM analyses (this preferred growth was also observed for apatites in gels[27–29]). Foreign phases or flaws were not observed between the glass matrix and the growing needle-like fluoroapatite crystals in the HRTEM analyses. Therefore, both of the needle-shaped crystals are fluoroapatite crystals that show almost ideal growth. This needle-like morphology of fluoroapatite is very similar to that of needle-like hydroxyl-carbonato apatite in human teeth (Fig. 20). Therefore, we concluded that fluoroapatite in glass-ceramics mimics natural apatite in respect to morphology.

Acknowledgements

Fig. 20 Hydroxy-carbonato apatite crystals of human tooth (enamel). SEM, etched sample (37% H$_3$PO$_4$, 30 s, Total Etch ®, Ivoclar Vivadent AG).

References

1 L. L. Hench, *J. Am. Ceram. Soc.*, 1991, **74**, 1487.
2 T. Kokubo, *Biomaterials*, 1991, **12**, 155.
3 L. L. Hench and J. M. Polak, *Science*, 2002, **295**, 1014.
4 J. C. Elliot, *Structure and properties of the apatites and other calcium phosphates*, Elsevier, Amsterdam, London, New York, Tokyo, 1994.
5 R. Z. Legeros and J. P. Legeros, in *An introduction to bioceramics*, ed. L. L. Hench and J. Willson, World Scientific, London, 1991, p. 139.
6 S. V. Dorozhkin, *J. Mater. Sci.*, 2007, **42**, 1061.
7 W. Höland, V. Rheinberger, E. Apel, C. van t' Hoen, M. Höland, A. Dommann, M. Obrecht and C. Mauth, *J. Mater. Sci.: Mater. Med.*, 2006, **17**, 1037.
8 W. Höland and G. H. Beall, *Glass-ceramic Technology*, ACS, Westerville, 2002; Wiley, New York, 2006.
9 W. Höland, *Glaskeramik*, UTB, Stuttgart, vdf Hochschulverlag an der ETH Zürich, Zürich, 2006.
10 W. Höland, M. Frank, M. Schweiger and V. Rheinberger, *Glastech. Ber. Glass Sci. Technol.*, 1994, **67C**, 117.
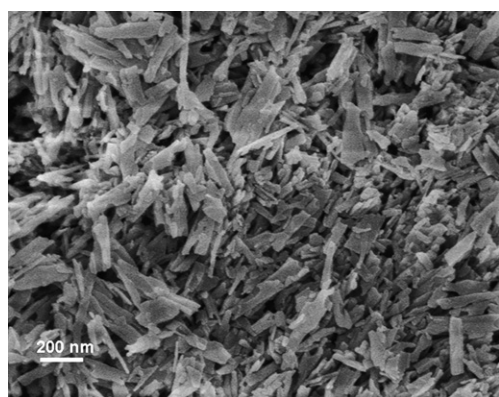11 A. Clifford and R. Hill, *J. Non-Cryst. Solids*, 1996, **196**, 346.

12 C. Moisescu, G. Carl and C. Rüssel, *Phosphorus Res. Bull.*, 1999, **10**, 515.
13 W. Höland, V. Rheinberger, S. Wegner and M. Frank, *J. Mater. Sci.: Mater. Med.*, 2000, **11**, 11.
14 M. Höland, A. Dommann, W. Höland, E. Apel and V. Rheinberger, *Glass Sci. Technol.*, 2005, **78**, 153.
15 W. Suchanek, M. Yashima and M. Kakihana, *J. Eur. Ceram. Soc.*, 1998, **18**, 1923.
16 E. Müller and F. Krumeich, *Ultramicroscopy*, 2000, **84**, 143.
17 C. P. Grey and A. J. Vega, *J. Am. Chem. Soc.*, 1995, **117**, 8232.
18 T. Gullion and J. S. Schaefer, *J. Magn. Reson.*, 1989, **81**, 196.
19 J. R. Garbow and T. Gullion, *J. Magn. Reson.*, 1991, **95**, 442.
20 K. Sudarsanan, P. E. Mackie and R. A. Young, *Mater. Res. Bull.*, 1972, **7**, 1331.
21 J. C. C. Chan, R. Ohnsorge, K. Meise-Gresch, H. Eckert, W. Höland and V. Rheinberger, *Chem. Mater.*, 2001, **13**, 4198.
22 E. Apel, W. Höland and V. Rheinberger, *Glastech. Ber. Glass Sci. Technol*, 2004, **77C**, 199.
23 M. Ben Amara, M. Vlasse, G. le Flem and P. Hagenmueller, *Acta Crystallogr., Sect. C*, 1983, **C39**, 1483.
24 R. Müller, L. A. Abu-Hilal, S. Reinsch and W. Höland, *J. Mater. Sci.*, 1999, **34**, 65.
25 W. Höland, V. Rheinberger and M. Frank, *J. Non-Cryst. Solids*, 1999, **253**, 170.
26 J. Schmedt auf der Günne, K. Meise-Gresch, H. Eckert, W. Höland and V. Rheinberger, *Glastech. Ber. Glass Sci. Technol.*, 2000, **73C1**, 90.
27 S. Busch, H. Dolhaine, A. Duchene, S. Heinz, O. Hochrein, F. Laeri, O. Podebrad, U. Vietze, T. Wieland and R. Kniep, *Eur. J. Inorg. Chem.*, 1999, 1643.
28 S. Busch, U. Schwarz and R. Kniep, *Chem. Mater.*, 2001, **13**, 3260.
29 R. Kniep and S. Busch, *Angew. Chem.*, 1996, **108**, 2788.